We are IntechOpen,
the world's leading publisher of
Open Access books
Built by scientists, for scientists

4,800

Open access books available

122,000

International authors and editors

135M

Downloads

154

Countries delivered to

Our authors are among the

TOP 1%

most cited scientists

12.2%

Contributors from top 500 universities

WEB OF SCIENCE™

Selection of our books indexed in the Book Citation Index
in Web of Science™ Core Collection (BKCI)

Interested in publishing with us?
Contact book.department@intechopen.com

Numbers displayed above are based on latest data collected.
For more information visit www.intechopen.com

Torque Sensors for Robot Joint Control

Dzmitry Tsetserukou and Susumu Tachi
University of Tokyo
Japan

1. Introduction

In the field of service robotics, there is a growing need for robots capable of physical interaction with humans to assist with daily life tasks. The desired coexistence of robotic systems and humans in the same physical domain (sharing the same workspace and actually cooperating in a physical manner) poses very fundamental problem of ensuring safety to the user and robot. Even without wrong programming, a robot, moving freely in a human environment, is potentially dangerous because of its large moving masses, powerful actuators, and unpredictably complex behavior. Design and programming of the robots exhibiting intrinsically safe behavior in a human domain are great challenges in robotics because such robots have to deal with unstructured time-varying environment. Several humanoid robots aimed at integration into people environment were developed (Sakagami et al., 2002), (Kaneko et al., 2004). However, despite the splendid means for sensing the environment (visual, audio, and haptics), the 6-axis force/torque sensors attached at the tip of the robot arm and a stereo vision system which is slow to track the changing environment in real-time, are only the abilities to anticipate and handle the collision. The rest parts of the robot body (forearm, elbow, upper arm, shoulder, and torso) are presenting the significant danger not only for human being, but also for the robot structure itself.

Effective methods on enhancement of contact detection ability of manipulator were reported. To avoid collisions in time-varying environment, Lumelsky & Cheung (2001) proposed to cover manipulator with a sensitive skin capable of detecting nearby objects. Mitsunaga et al. (2006) progressively improved the tactile ability of the robot through covering its entire body with piezoelectric-film-based tactile sensors. Since this device integrates a huge amount of small sensors incorporated into soft layer and requires the complicated wiring and signal processing hardware, it has high cost and reliability issues. The high-speed vision system attached to the robot arm aimed at real-time collision avoidance (Morikawa et al., 2007) presumes usage of expensive detectors, complex signal processing techniques, and issues of self-body extraction from the camera view area.

Is should be noted, that such tasks under human supervision as transporting the object, leading the robot tip via force-following, performing the assembling tasks, require the processing algorithm of contact state. Finding the technical solution for trade-off between performance and safety is the target of a new manipulation technology. To cope with this issue, an active compliance control implying fast joint torque controlling based on measuring the applied external torque in each joint was developed. The first embodiment of torque measurement is the integration of a torque sensor into each joint of the manipulator.

The impedance control generates compliant trajectory based on information on the measured external torque. Such approach has two main advantages: (1) sensor detects not only forces applied to the hand but also those exerted at other points on the manipulator, (2) and allows to increase the performance of fast movements by active vibration damping. Several attempts have been made by researchers to improve joint torque control. Wu & Paul (1980) proposed a simple, wide bandwidth, torque servo system using strain-gauge-based joint torque sensor. The torque-controlled lightweight robot arm with high load to weight ratio was developed by Hirzinger et al. (2001). Each joint of the arm is facilitated with strain-gauge-based torque sensor, position sensor and piezzo-brake. Sakaki & Iwakane (1992) proposed to use a compact motor drive with embedded magnetostrictive torque sensor for impedance control of the robot arm. The approach of torque measurement through the elasticity of the harmonic drive flexsplines allows keeping the same stiffness and mechanical structure of the robot (Hashimoto et al., 1993), (Golder et al., 2001). This method requires the strain gauges to be installed on the flexsplines. The crucial shortcomings of the torque measurement approaches mentioned above will be discussed in Section 2.

The alternative method for increasing the safety level of robot arms interacting with humans is intentionally introducing compliance at the mechanical design level (passive control). The main idea here is decoupling the rotor inertia from the link inertia through use of passive elasticity (Bicchi & Tonietti, 2004). However, the robot control is complicated by many unknown parameters (e.g. actuator stiffness and damping). Furthermore, compliant transmission negatively affects the performance in term of increased oscillations and settling time.

To realize the safe physical contact of entire robot arm structure with human and to guarantee the collision avoidance, our primary idea is concentrated on the design of a whole-sensitive robot arm (by using distributed torque sensors in each joint). When contact with environment occurs, manipulator automatically generates compliant motion according to the measured external torque and time derivative of torque.

The Chapter is devoted to the design of new optical torque sensors and robot joint control system for safe physical interaction with surroundings.

2. Background of torque measurement techniques

The torque transducer on the motor shaft includes a load cell structure supporting the load and deflecting a known amount in response to applied torque. Deformation of the elastic element is measured in different ways as follows:
1. *Electrically.*
2. *Based on electromagnetic phenomena.*
3. *Optically.*

These approaches include: 1) noncontact transducers measuring relative displacement by light radiation detection, Hall effect, Faraday's law, and 2) contacting transducers measuring strain by means of strain gauges, potentiometers, piezoelectric effect, optical fibre.

2.1 Electrical methods
Electrical measurement is essentially associated with strain gauges, capacitive, and piezoelectric sensing. Strain gauge operation is based on variations in electrical resistance with strain. When force is applied, strain changes the electrical resistance of gauges proportionally to the load. Silicon semiconductor strain gauges are often used due to high

sensitivity. Strain in silicon causes its bulk resistance to change, producing a signal 75 times stronger than conventional foil gauges where resistance changes are only due to dimensional changes in the resistor. Despite such benefits of strain gauges as high linearity, about 0.03%-2.5% of full scale (FS), high resolution of 1-3 mV/V, their maximum allowable strain is close to their breaking point. To guarantee overload protection of transducers, mechanical stops limiting deflections of flexures are necessary. Very stiff sensors may only deflect a few ten-thousandths of a millimeter. Production of limit stops with such small clearances is very difficult. Strain-gauge-based torque/force sensors are greatly subjected to radial and other force components. Semiconductor and foil gauges require elaborate process for attachment by a specialist. Another shortcoming of these sensors is their high sensitivity to electrical noise and temperature (Westbrook & Turner, 1994).

Piezoelectric torque sensors are similar in operation to strain gauges and based on the phenomenon, in which a crystal becomes electrically charged under the action of mechanical stress. High stiffness and strength enable sensors to be directly inserted into the torsion member. An example of the piezoelectric effect is the invention (Kovacich et al., 2002), where authors exploited changes in the resonant frequency of the piezoelectric element as a measure of the strain, to which the torsion member is subjected. Extremely high accuracy (0.03% of FS) and high signal output are their main advantages. Drawbacks restricting their application are high cost and nonlinear output.

Many torque transducers are based on measuring the relative angle between the two ends of the torsion bar. This principle was realized in the differential capacitive sensor for measurement of the relative angle (Fulmek et al., 2002). The transducer is noncontact, robust, and compact. Two rotatable electrodes are placed between two sensor plates. The relative angle between the two rotors and the absolute position of the rotor blades are calculated from measurement of capacitive coupling between different transmitting stator segments and a single receiving electrode. Its drawback is high sensitivity to radial displacement and high cost. The relationship between the capacitor capacity and permittivity of the dielectric material between the capacitor plates also was used in patent (Madni et al., 2004). In this invention, the apertured metal cage shielding a dielectric rotor is placed between capacitor plate rings fixed on opposite sides of a torsion bar. The relative rotation of the apertured conductive plates and the dielectric rotor changes the overall differential capacitance of the system in proportion to torque.

2.2 Electromagnetic phenomena

Faraday's law (inductive sensors), magnetostriction, and magnetoelastic effect are used in electromagnetic sensors. Vischer & Khatib (1995) used linear variable differential transformers (LVDT) in the torque sensor. The hub-spoke structure of this torque sensor is given in Fig. 1 (reference numeral 1 denotes a flexible beam, 2 denotes a LVDT).

The main advantage of LVDT is their high degree of robustness, remarkable resolution of about 0.1μm, good accuracy (0.01-0.3%), and easy installation and calibration. High reliability is derived from their operation principle based on magnetic transfer eliminating physical contact across the sensing element. The strong relationship between core position and output voltage of secondary coils yields excellent resolution. Inductive sensors suffer from reduction in signal at very low frequencies, and they are affected by electromagnetic noise. The smallest LVDT made by the Lucas Schaevitz in XS-B series weighs only 4.36 g and has an outer diameter of 4.77 mm, but its length of 22.4 mm complicates compact overall dimensions of the torque transducer.
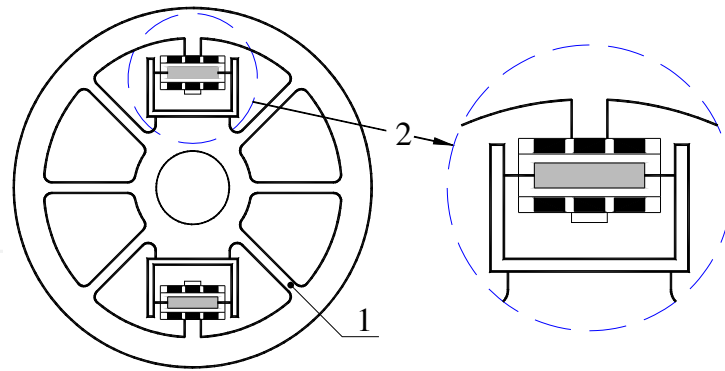
Fig. 1. Six-beam torque sensor with LVDT transducer (Vischer & Khatib, 1995)

The effect, in which stress applied to the material causes a change in its magnetization, is known as the Villari effect or magnetostriction phenomena. Magnetostrictive torque sensors consist of rotational shaft, having a magnetostrictive metal layer of a chevron configuration formed on the shaft, an exiting coil, and a pickup coil for detecting the magnetic property change of the magnetostrictive layer. When AC current is applied to the exciting core, the magnetostrictive layer is excited. Torque applied to the magnetostrictive element generates stress. Permeability is changed by the Villari effect, and inductive output is generated in the pickup coil with torsional load (Shinoura, 2003). Advantages of the sensor are nonphysical contact between the shaft and housing, and high torsional stiffness. Drawbacks are complicated manufacturing, bulky heavy structure, need for a robust magnetic shield, and insufficient performance (linearity of 3-5% FS, hysteresis of 2-3%, resolution of 10 mV/V) (Ishino et al., 1996).

2.3 Optical approaches

A light source, photosensor, and solid object modifying the amount of light incident on the optical detector are necessary to measure displacement between unmovable and flexible parts of the optical sensor. Photosensors have such drawbacks as nonlinearity and temperature sensitivity, but they are considerably more reliable, cheap, and simplified in design than other sensors. A displacement is detected by interrupting light between source and detector, changing the intensity of reflected light, or the relative movement of source and detector. Hirose & Yoneda (1990) have significantly contributed to research on the optical force/torque sensors. They proposed using a split photosensor to detect displacement of the light source (LED) caused by applied force in two directions. This sensor is shown in Fig. 2 (1 denotes a force loaded adapter plate, 2 denotes a load cell (elastic element), 3 denotes a photodetector, 4 denotes a LED, 5 denotes an installation adapter plate).

When force is applied to the plate 1, elastic solid body 2 deflects LED light incident on photosensor 3. Thus, magnitude of the photodetector output responds on exerting force/moment. In cooperation with the Minebea Co., OPFT series of 6-axis optical force/torque sensors were manufactured (Minebea). Compared to conventional strain-gauge-based transducers, they are more compact, lightweight, and cheap, but they have complicated calibration due to nonlinear output, require application of DSP for real-time computation of measured force, and have an average accuracy of 5% FS.

At Nara Institute of Science and Technology, a 6-axis optical force/torque sensor was developed for fMRI application (Takahashi et al., 2003). The sensor was made from acrylic resin to eliminate any metal sensor components that generate fMRI signal noise. The layout

of the transducer is shown in Fig. 3. The elastic frame has a Y-topology with S-shaped beams to enable 6-DOF displacement of the sensing face. Force exerted by users deflects the elastic frame, altering the intensity of light falling on optical fiber. The sensor provides accuracy of 2.65% for measurement of moment M_Z. The transducer is complicated and intended only for narrow applications.
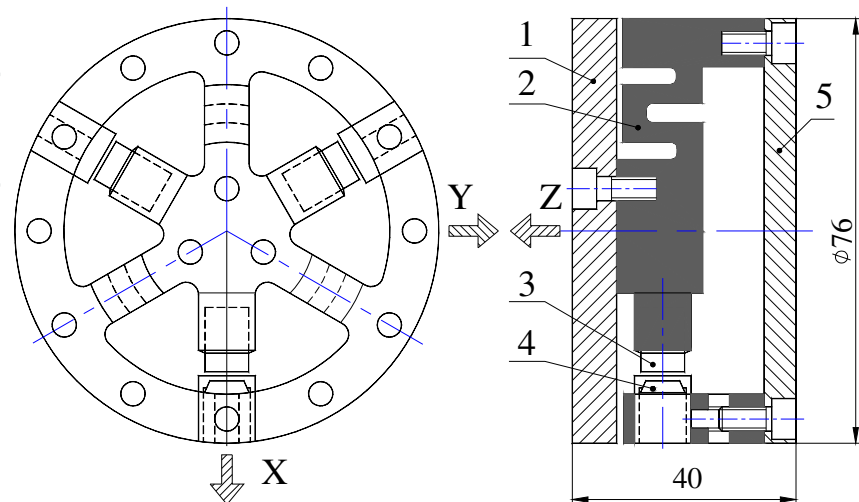

Fig. 2. Layout of the 6-axis optical force/torque sensor (Hirose & Yoneda, 1990)

The idea of the patent (Okutani & Nakazawa, 1993) is calculation of torque by measuring the angle of twist of the torsion shaft through detection of differences in the rotation position of disks at opposite sides of the torsion shaft using an optical encoder. The encoder-type torque sensor suffers from large overall dimensions and requires very precise relative installation of apertured disks. To overcome this, the author (Horton, 2004) invented a torque sensor including a source of optical radiation, a two-dimensional array of a radiation detector and two modulating apertured disks placed between the source and detector. When torque is applied to the shaft, the relative position between disks alters overlapping slots and hence the size of the apertures, which control the pattern of light incident upon the optical detector.
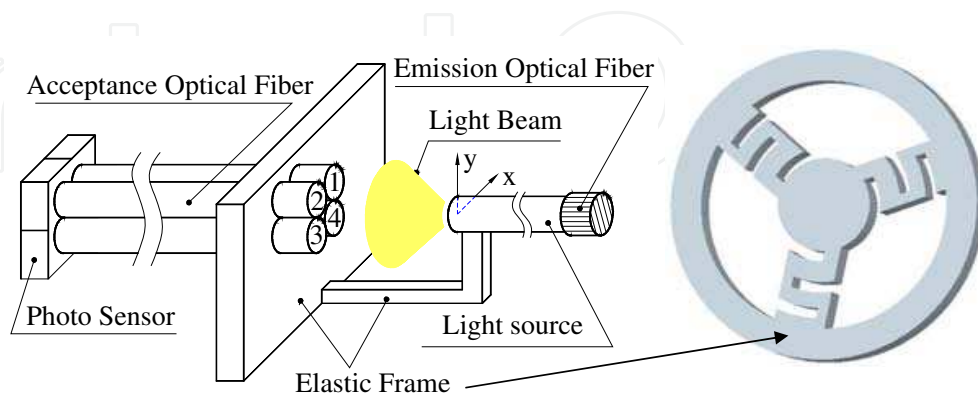

Fig. 3. Layout of the 6-axis optical force/torque sensor (Takahashi et al., 2003)

The 6-axis force/torque converter using LEDs and photodiodes is described in (Hilton, 1989).

3. Development of a new optical torque sensor

3.1 Senor specifications

The specific application (i.e. robot arm interacting with human beings in a safe manner) introduces special requirements to the design of torque sensor. New anthropomorphic robot arm iSoRA (**i**ntelligent **So**ft **R**obot **A**rm) enabling integration of torque sensors was developed. The 3D model of the robot arm, cross-section of the shoulder joint with built-in torque sensors, and frame assignments are shown in Fig. 4.
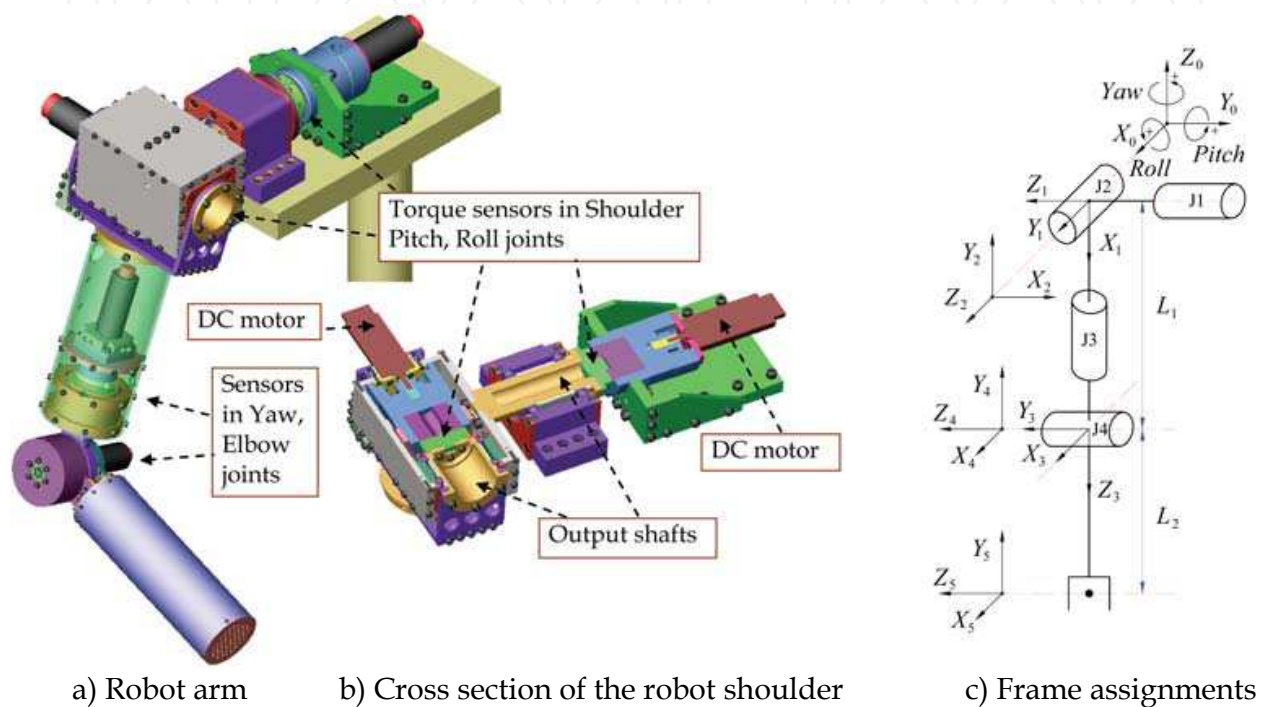

a) Robot arm   b) Cross section of the robot shoulder   c) Frame assignments

Fig. 4. 3D model of the new anthropomorphic robot arm

The list of desirable properties of torque sensor aimed at integration into anthropomorphic robot arm is given below.

1. Addition of the torque sensor to a robot joint should not require redesign of the joint and should cause minimal modification in kinematics and dynamics. Therefore, lightweight sensor with small width is preferable.
2. Noise created by current passing through the DC motor at each joint of the robot arm should not affect the sensing element, and usage of electromagnetic sensors should be avoided in this application.
3. The angle of twist of the movable part of the transducer at the maximum expected external torque should enable exploiting as wide range of detector sensitivity as possible to achieve high signal-to-noise ratio and sensor resolution.
4. Torsional stiffness of the sensor should not considerably reduce the natural frequency of the robot arm and deteriorate the position accuracy. This introduces the trade-off in stiffness maximization while maintaining high sensitivity.
5. Another difficulty in design of the torque sensor is hysteresis elimination. Most metals used as flexures have very little hysteresis. Bolted, press fit, and welded joints near the flexure introduce hysteresis. Hence, mechanical structure should be machined from a single piece of metal.

6. Influence from any of the nontorsional components of load should be canceled to guarantee precise measurement of torque T that is moment around Z-axis M_Z in 6-axis sensors.
7. Behavior of the sensing element output and mechanical structure should be as close to linear as possible.
8. Simple to manufacture, low-cost, and robust.

Optical approaches of torque measurement satisfy the demands of compact sizes, light in weight, and robustness. The small influence of electrical noise created by DC motors on output signal of optical sensors results in high signal-to-noise ratio and sensor resolution. Therefore, we decided to employ this technique to measure torque in robot joints.

3.2 Design of new optical torque sensors

The novelty of our method is application of the ultra-small size photointerrupter (PI) as sensitive element to measure relative motion of sensor components. The relationship between the output signal and position of the shield plate for RPI-121 (ROHM) is shown in Fig. 5. The linear section of the transferring characteristic corresponding approximately to 0.2 mm is used for detection of the relative displacement of the object. The dimensions of the photointerrupter (RPI-121: 3.6 × 2.6 × 3.3 mm) and weight of 0.05 g enable realization of compact sensor design.
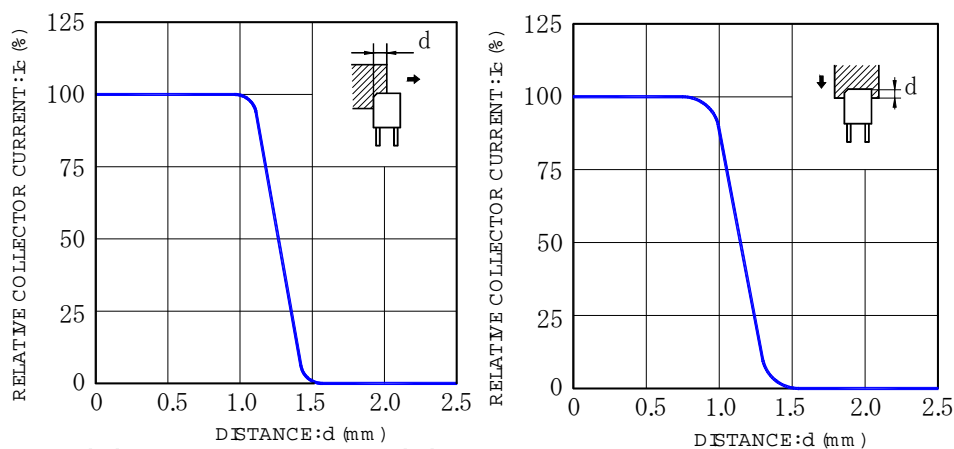

Fig. 5. Relative output vs. Distance (ROHM)

Two mechanical structures were realized to optimize the sensor design: the in-line structure, where detector input and output are displaced axially by the torsion component; and the "in plane" one, where sensor input and output are disposed in one plane and linked by bending radial flexures. The layout of the in-line structure based on a spring with a cross-shaped cross section is shown in Fig. 6. This spring enables large deflections without yielding. The detector consists of input part 1, output part 2, fixed PI 3, shield 4, and cross-shaped spring 5. The operating principle is as follows: when torque T is applied to the input shaft, the spring is deflected, rotating the shield 4. Shield displacement is detected by the degree of interruption of infrared light falling on the phototransistor. The magnitude of the PI output signal corresponds to the applied torque. The "in plane" arrangement of the load cell was designed to decrease the sensor thickness and, therefore, to minimize modification in dimensions and weight of robot joint.

The layout of the structure having hub and three spokes (Y-shaped structure) and 3D 3D assembly model are shown in Fig. 7. The detector consists of inner part 1 connected by flexure 3 with outer part 2, fixed PI 5, slider with shield plate 4, and screws 6. When torque is applied, radial flexures are bent. The shield is adjusted by rotating oppositely located screws 6. The pitch of screws enables smooth movement of the slider along with the shield plate.
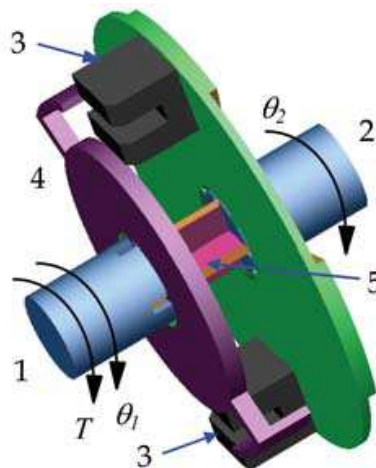

Fig. 6. Construction of the optical torque sensor
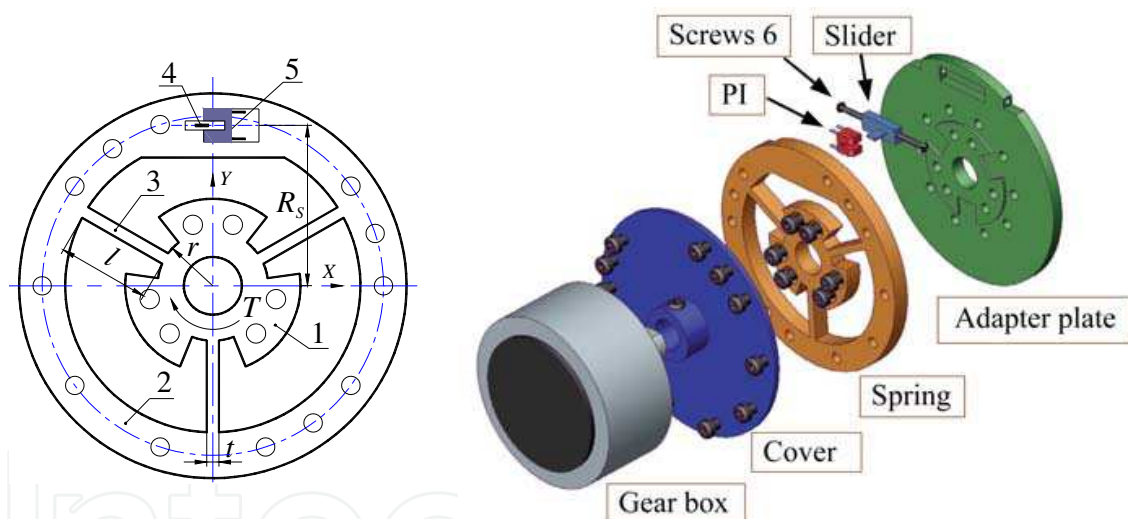
Fig. 7. Layout of hub-spoke spring and position regulator

The relationship between the applied torques to robot arm structure and the resultant angles of twist for the case of linear elastic material is as follows:

$$T = k\theta = k\left(\theta_{in} - \theta_{out}\right),$$ (1)

where $T = [\tau_1, \tau_2, ..., \tau_n]^T \in R^n$ is the vector of applied joint torques (Nm); $k = [k_1, k_2, ..., k_n]^T \in R^n$ is the vector of torsional stiffness of the flexures (Nm/rad); $\theta = [\theta_1, \theta_2, ..., \theta_n]^T \in R^n$ is the vector of angles of twist (rad), θ_{in} is the vector of angles of input shaft rotation; θ_{out} is the vector of angles of output shaft rotation.

Since the angle of twist is fairly small, it can be calculated from the displacement of the shield in tangential direction Δx, then Eq. (1) becomes:

$$T = k\Delta x / R_s \,, \tag{2}$$

where R_S is the vector of distances from the sensor axis to the middle of the shield plate in radial direction.

Sensor structure rigidity can be increased by introducing additional evenly distributed spokes (Nicot, 2004). The torsional stiffness of this sensor is derived from:

$$k = 4NEI\left(\frac{1}{l} + \frac{3r}{l^2} + \frac{3r^2}{l^3}\right), \tag{3}$$

where N is the number of spokes, l is the spoke length, E is the modulus of elasticity, r is the inner radius of the sensor (Vischer & Khatib, 1995).

The moment of inertia of spoke cross section I is calculated as:

$$I = \frac{bt^3}{12}, \tag{4}$$

where b is the beam width, t is the beam thickness.

The sensor was designed to withstand torque of 0.8 Nm. The results of analysis using FEM show von Mises stress in MPa under a torque T of 0.8 Nm (Fig. 8a), tangential displacement in mm (Fig. 8b), von Mises stress under a bending moment M_{YZ} of 0.8 Nm (Fig. 8c), and von Mises stress under an axial force F_Z of 10 N (Fig. 8d).

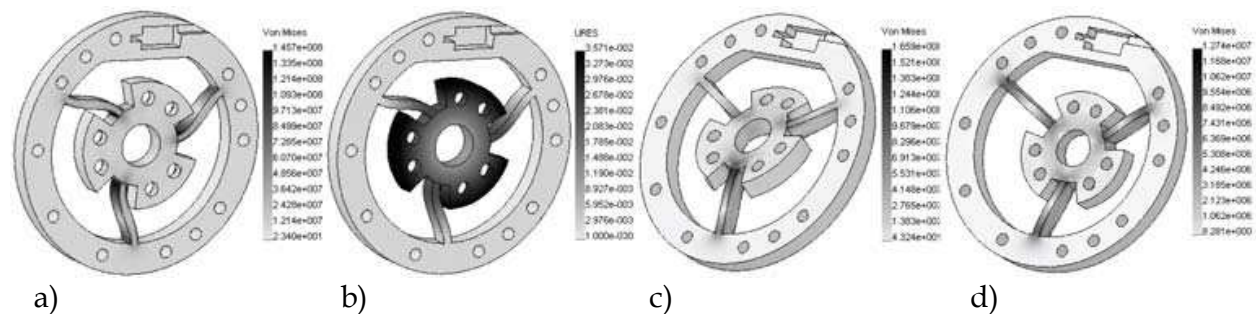a)   b)   c)   d)

Fig. 8. Results of analysis of hub-spoke spring using FEM

The maximum von Mises stress under torque T of 0.8 Nm equals $\sigma_{MaxVonMises} = 14.57 \cdot 10^7$ N/m^2 < $\sigma_{yield} = 15.0 \cdot 10^7$ N/m^2. The angle of twist of 0.209° is calculated from the tangential displacement. The ability to counteract bending moment is estimated by the coefficient:

$$K_{TM} = \frac{\sigma_{MaxVonMises(T)}}{\sigma_{MaxVonMises(M_{YZ})}}. \tag{5}$$

The hub-spoke spring coefficient K_{TM} equals 0.878. To estimate the ability to counteract axial force F_Z, the same approach is applied:

$$K_{TF} = \frac{\sigma_{MaxVonMises(T)}}{\sigma_{MaxVonMises(F_Z)}}. \tag{6}$$

After substitution of magnitudes, we calculate $K_{TF} = 11.44$. Our sensor was machined from one piece of brass using wire electrical discharge machining (EDM) cutting to eliminate

hysteresis and guarantee high strength (Fig. 9). In this sensor, the ultra-small photointerrupter RPI-121 was used. We achieved as small thickness of the sensor as 6.5 mm.
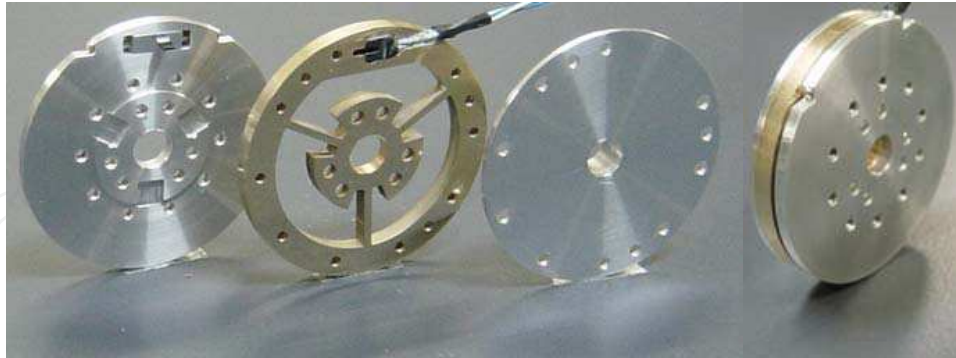

Fig. 9. Optical torque sensor with hub-spoke-shaped flexure

The ring-shaped spring was designed to extend the exploiting range of the PI sensitivity while keeping same strength and outer diameter. Layout and 3D assembly model of the developed optical torque sensor are shown in Fig. 10 (1 designates a shield plate, 2 designates a PI RPI 131, 3 designates a ring-shaped flexure). The flexible ring is connected to the inner and outer parts of the sensor through beams. Inner and outer beams are displaced with an angle of 90° that enables large compliance of the ring-shaped flexure.
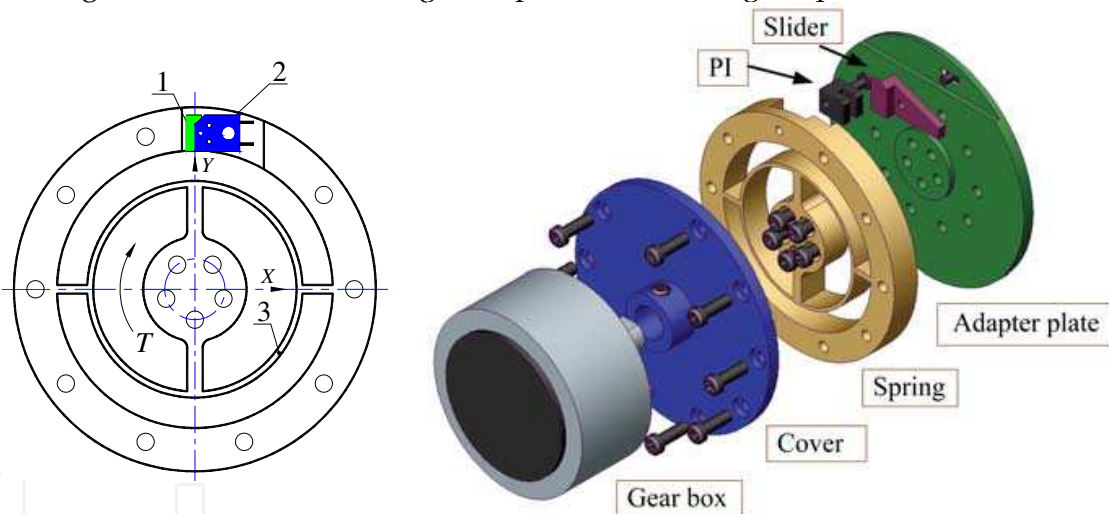

Fig. 10. Ring-shaped topology of the spring

The results of analysis using FEM show von Mises stress in MPa under torque T of 0.8 Nm (Fig. 11a), tangential displacement in mm (Fig. 11b), von Mises stress under bending moment M_{YZ} of 0.8 Nm (Fig. 11c), and von Mises stress under axial force F_Z of 10 N (Fig. 11d).

The maximum von Mises stress under torque T of 0.8 Nm equals $\sigma_{MaxVonMises}$= 8.74·10^7 N/m^2 < σ_{yield} = 8.96·10^7 N/m^2. Given structure provides the following coefficients: K_{TM} = 0.217, K_{TF} = 3.56, and angle of twist θ of 0.4°. Thus, the ring-shaped structure enables magnifying the angle of twist deteriorating the degree of insensitivity to bending torque and axial force. This structure was machined from one piece of aluminium A5052. The components and assembly of the optical torque sensor are shown in Fig. 12. The sensor thickness is 10 mm. The displacement of the shield is measured by photointerrupter RPI-131. The shortcomings of this design are complicated procedure of adjusting the position of the shield relatively photosensor and deficiency of the housing to prevent the optical transducer from damage.
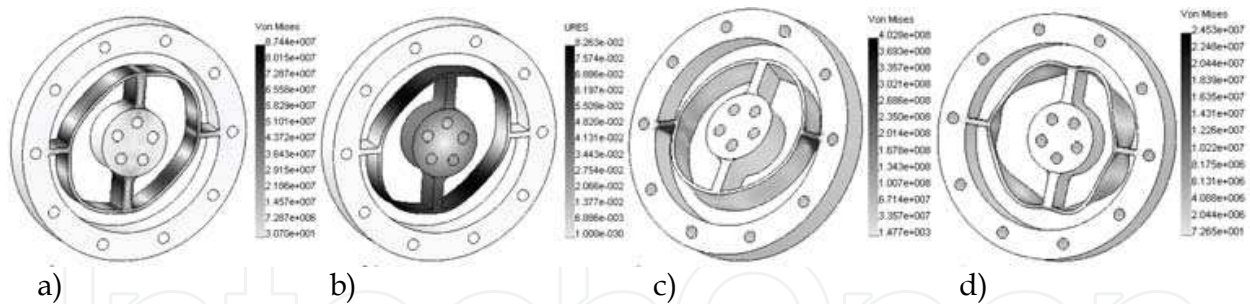
Fig. 11. Result of analysis of ring-shaped flexure using FEM

Fig. 12. Optical torque sensor with ring-shaped flexure

The sensor with a ring topology was modified. The layout of the detector with semicircular flexure and 3D model are given in Fig. 13 (1 designates a shield, 2 designates a PI RPI-121, 3 designates a semicircular flexure).
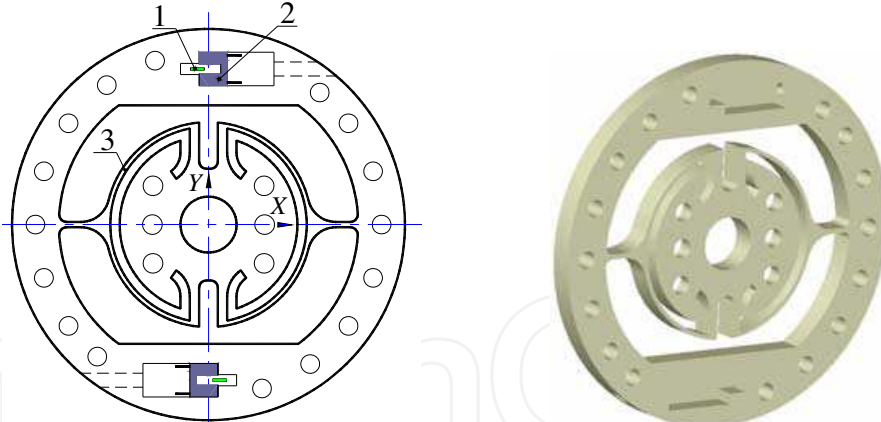

Fig. 13. Semi-ring-shaped spring

The results of analysis using FEM show von Mises stress in MPa under torque T of 0.8 Nm (Fig. 14a), tangential displacement in mm (Fig. 14b), von Mises stress under bending moment M_{YZ} of 0.8 Nm (Fig. 14c), and von Mises stress under axial force F_Z of 10 N (Fig. 14d).

The maximum von Mises stress under maximum loading is less then yield stress $\sigma_{MaxVonMises} = 14.94 \cdot 10^7$ N/m² < $\sigma_{yield} = 15.0 \cdot 10^7$ N/m². The semicircular flexure provides the following coefficients: $K_{TM} = 0.082$, $K_{TF} = 2.83$, and angle of twist θ of 0.39°. This structure was machined from one piece of brass C2801. The sensor is 7.5 mm thick. Its drawback is high sensitivity to bending moment. Components and assembly of this optical torque sensor are shown in Fig. 15.
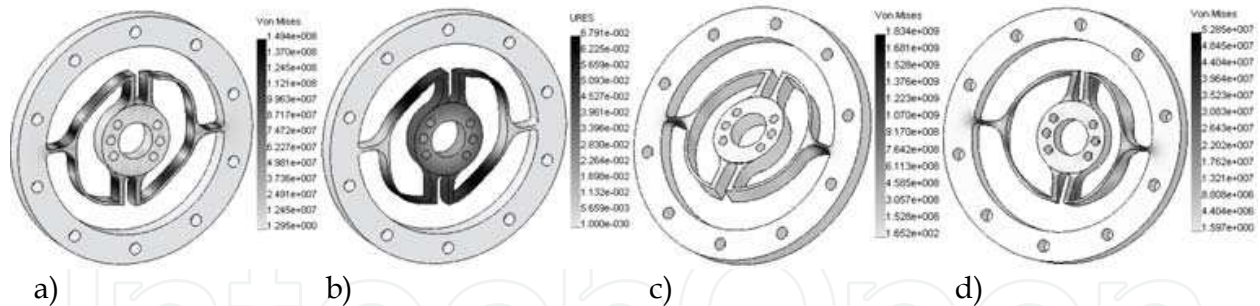
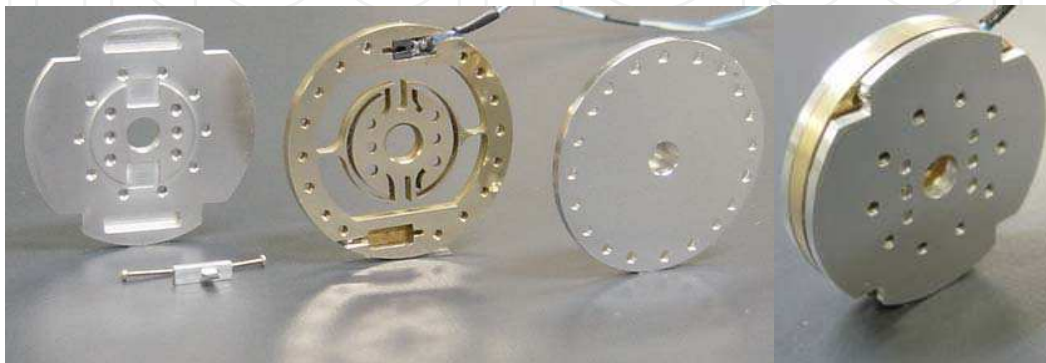Fig. 14. Results of analysis of semi-ring-shaped spring using FEM

Fig. 15. Optical torque sensor with semi-ring-shaped flexure

In the test rig for calibrating the optical sensor (Fig. 16), force applied to the arm, secured by screws to the rotatable shaft, creates the loading torque. Calibration was realized by incrementing the loading weights and measuring the output signal from the PI. Calibration plots indicate high linearity of the sensors output signal.
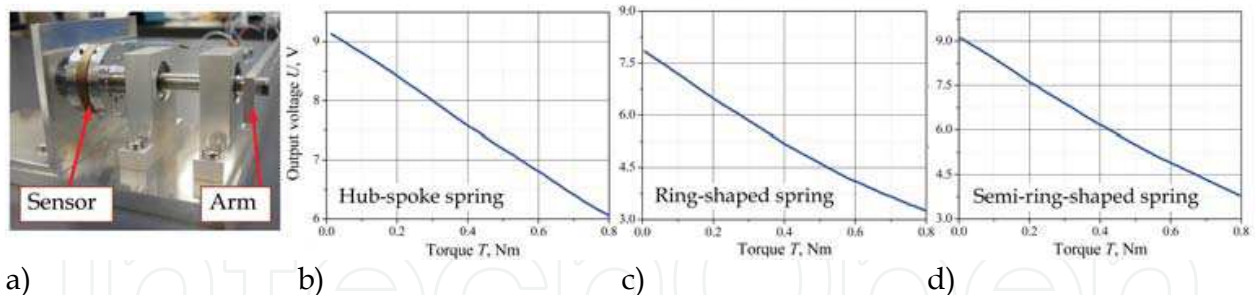

Fig. 16. Test rig and calibration result

Technical specifications of optical torque sensors are listed in Table 1.

The technical specifications of 6-axis force/torque sensors with a similar sensing range of torque around Z-axis are listed in Table 2 (ROHM), (ATI), (BL AUTOTEC).

The spoke-hub topology enables a compact and lightweight sensor. The large torsional stiffness does not considerably deteriorate the dynamic behavior, but diminishes PI resolution. The semicircular spring has high sensitivity to bending moment and axial force and small natural frequency. As regards the ring-shaped flexure, it provides wide torsional stiffness with high mechanical strength. The main shortcoming of this topology is high sensitivity to bending moment. Nevertheless, this obstacle is overcome through realization of a simple supported loading shaft of the robot joint. In the most loaded joints, e.g.

shoulder, such material as hardened stainless steel can be used for elastic elements to keep sensor dimensions the same. Compared to strain-gauge-based sensor ATI Mini 40, our optical sensors have small torsional stiffness and low factor of safety. However, such advantages of designed sensors as low cost, easy manufacture, immunity to the electro-magnetic noise, and compactness make them preferable for torque measurement in robot arm joints. The linear transfer characteristic of the PI simplifies calibration of the sensor. Because of sufficient stiffness, high natural frequency, small influence of bending moment and axial force on the sensor accuracy, the hub-spoke spring as deflecting part of the optical torque sensor was chosen. Four torque sensors for integration into robot joints were manufactured and calibrated (Tsetserukou et al., 2007). The sensors were installed between the harmonic drives and driven shafts of the robot joints.

Sensor	Hub-spoke spring	Ring-shaped spring	Semicircular spring
Spring member material	Brass C2801	Aluminium A5052	Brass C2801
Photointerrupter type	RPI-121	RPI-131	RPI-121
Load capacity, Nm	0.8	0.8	0.8
Torsional stiffness, Nm/rad	219.8	115.86	116.99
Natural frequency, kHz	5.25	2.7	1.37
Factor of safety	1.0	1.0	1.0
Outer diameter, mm	42	42	42
Thickness, mm	6.5	10.0	7.5
Sensor mass, g	34.7	28.7	36.8

Table 1. Technical specifications

Sensor	ATI Mini 40 Hub-spoke spring	BL Autotec Mini 2/10 Hub-spoke spring	Minebea OPFT-50N Hub-spoke spring
Spring member material	Hardened stainless steel	Stainless steel	Aluminium
Sensing element	Silicon strain gauge	Strain gauge	LED-Photodetector
Sensing range MZ, Nm	1.0	1.0	2.5
Torsional stiffness Z-axis, Nm/rad	4300	-	-
Natural frequency, kHz	3.2	-	-
Accuracy, %	-	1.0	5.0
Factor of safety	5.0	5.0	1.5
Outer diameter, mm	40	40	50
Thickness, mm	12.25	20	31.5
Sensor mass, g	50	90	133

Table 2. Technical specifications of the 6-axis force sensors

4. Robot arm control

4.1 Joint impedance control

The dynamic equation of an *n*-DOF manipulator in joint space coordinates (during interaction with environment) is given by:

$$M(\theta)\ddot{\theta} + C(\theta,\dot{\theta})\dot{\theta} + \tau_f(\dot{\theta}) + G(\theta) = \tau + \tau_{EXT}, \tag{7}$$

where $\theta, \dot{\theta}, \ddot{\theta}$ are the joint angle, the joint angular velocity, and the joint angular acceleration, respectively; $M(\theta) \in R^{n \times n}$ is the symmetric positive definite inertia matrix; $C(\theta, \dot{\theta}) \in R^n$ is the vector of Coriolis and centrifugal terms; $\tau_f(\dot{\theta}) \in R^n$ is the vector of actuator joint friction torques; $G(\theta) \in R^n$ is the vector of gravitational torques; $\tau \in R^n$ is the vector of actuator joint torques; $\tau_{EXT} \in R^n$ is the vector of external disturbance joint torques.

People can perform dexterous contact tasks in daily activities, regulating own dynamics according to time-varying environment. To achieve skillful human-like behavior, the robot has to be able to change its dynamic characteristics depending on time-varying interaction forces. The most efficient method of controlling the interaction between a manipulator and an environment is impedance control (Hogan, 1985). This approach enables to regulate response properties of the robot to external forces through modifying the mechanical impedance parameters. The graphical representation of joint impedance control is given in Fig. 17.
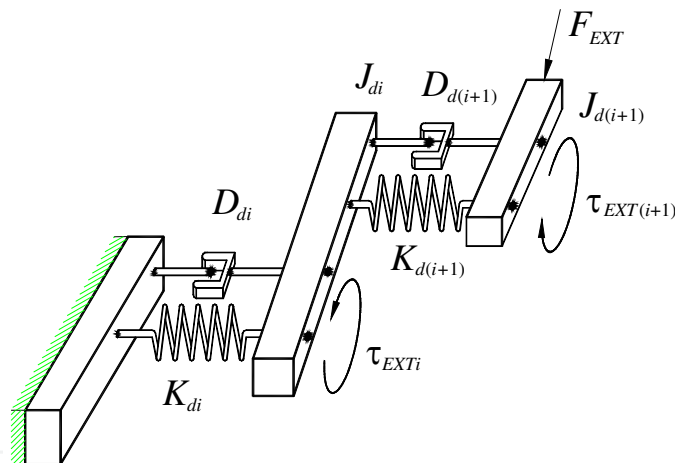

Fig. 17. Concept of the local impedance control

The desired impedance properties of *i-th* joint of manipulator can be expressed as:

$$J_{di}\Delta\ddot{\theta}_i + D_{di}\Delta\dot{\theta}_i + K_{di}\Delta\theta_i = \tau_{EXTi}; \ \Delta\theta_i = \theta_{ci} - \theta_{di}, \tag{8}$$

where J_{di}, D_{di}, K_{di} are the desired inertia, damping, and stiffness of *i-th* joint, respectively; τ_{EXTi} is torque applied to *i-th* joint and caused by external forces, $\Delta\theta_i$ is the difference between the current position θ_{ci} and desired one θ_{di}. The state-space presentation of the equation of local impedance control is written as follows:

$$\begin{bmatrix} \Delta\dot{\theta}_i \\ \dot{v}_i \end{bmatrix} = \begin{bmatrix} 0 & 1 \\ -K_d/J_d & -D_d/J_d \end{bmatrix} \begin{bmatrix} \theta_i \\ v_i \end{bmatrix} + \begin{bmatrix} 0 \\ 1/J_d \end{bmatrix} \tau_{EXTi}(t), \tag{9}$$

or:

$$\begin{bmatrix} \Delta\dot{\theta}_i \\ \dot{v}_i \end{bmatrix} = A \begin{bmatrix} \theta_i \\ v_i \end{bmatrix} + B\tau_{EXTi}(t) \text{ ,} \tag{10}$$

where the state variable is defined as $v_i = \Delta\dot{\theta}_i$; A, B are matrices. After integration of Eq. (10), the discrete time presentation of the impedance equation is expressed as:

$$\begin{bmatrix} \Delta\theta_{k+1} \\ \Delta\dot{\theta}_{k+1} \end{bmatrix} = A_d \begin{bmatrix} \Delta\theta_k \\ \Delta\dot{\theta}_k \end{bmatrix} + B_d T_{EXT(k)} . \tag{11}$$

To achieve the fast non-oscillatory response on the external force, we assigned the eigenvalues λ_1 and λ_2 of matrix A as real and unequal $\lambda_1 \neq \lambda_2$. By using Cayley-Hamilton method for matrix exponential determination, we have:

$$A_d = e^{AT} = \frac{1}{\lambda_1 - \lambda_2} \begin{bmatrix} e^{\lambda_2 T}\lambda_1 - e^{\lambda_1 T}\lambda_2 & e^{\lambda_1 T} - e^{\lambda_2 T} \\ -b\left(e^{\lambda_1 T} - e^{\lambda_2 T}\right) & e^{\lambda_2 T}\left(\lambda_1 + a\right) - e^{\lambda_1 T}\left(\lambda_2 + a\right) \end{bmatrix}, \tag{12}$$

$$B_d = \left(A_d - I\right)A^{-1}B = -\frac{c}{b\left(\lambda_1 - \lambda_2\right)} \begin{bmatrix} e^{\lambda_2 T}\lambda_1 - e^{\lambda_1 T}\lambda_2 - \left(\lambda_1 - \lambda_2\right) \\ -b\left(e^{\lambda_1 T} - e^{\lambda_2 T}\right) \end{bmatrix}, \tag{13}$$

where T is the sampling time; coefficients a, b, and c equal to D_d/M_d, K_d/M_d, and $1/M_d$, respectively; I is the identity matrix.
The eigenvalues λ_1 and λ_2 can be calculated from:

$$\lambda_1 = \frac{-a + \sqrt{a^2 - 4b}}{2}; \quad \lambda_2 = \frac{-a - \sqrt{a^2 - 4b}}{2} . \tag{14}$$

The value of contact torque τ_{EXTi} defines the character of joint compliant trajectory $\Delta\theta_i, \Delta\dot{\theta}_i$.

In addition to contact force, torque sensor continuously measures the gravitational, inertial, friction, Coriolis, and centrifugal torques (Eq. (7)). The plausible assumptions of small speed of joint rotation and neglible friction forces allow us to consider only gravitational torques. To extract the value of the contact force from sensor signal, we elaborated the gravity compensation algorithm.

4.2 Gravity compensation
In this subsection, we consider the problem of computing the joint torques corresponding to the gravity forces acting on links with knowledge of kinematics and mass distribution. It is assumed that due to small operation speed the angular accelerations equal zero. The Newton-Euler dynamics formulation was adopted. In order to simplify the calculation procedure, the effect of gravity loading is included by setting linear acceleration of reference frame $^0\dot{\vartheta}_0 = G$, where G is the gravity vector. First, link linear accelerations $^{i+1}\dot{\vartheta}_{C_{i+1}}$ of the center of mass (COM) of each link are iteratively computed from Eq. (15). Then,

gravitational forces $^{i+1}F_{i+1}$ acting at the COM of the first and second link are derived from Eq. (16):

$$^{0}\dot{\vartheta}_{0} = g\hat{Z}_{0}; \quad ^{i+1}\dot{\vartheta}_{C_{i+1}} = {}^{i+1}R_{i}^{i}\dot{\vartheta}_{i} \qquad (15)$$

$$^{i+1}F_{i+1} = m_{i+1}^{\ \ i+1}\dot{\vartheta}_{C_{i+1}}, \qquad (16)$$

where m_{i+1} is mass of the link $i+1$, $^{i+1}R_{i}$ is matrix of rotation between successive links calculated using Denavit-Hartenberg notation.

While inward iterations, we calculate force $^{i}f_{i}$ (Eq. (17)) and moment $^{i}n_{i}$ (Eq. (18)) acting in the coordinate system of each joint. In the static case, the joint torques caused by gravity forces are derived by taking Z component of the torque applied to the link (Eq. (19)).

$$^{i}f_{i} = {}_{i+1}^{i}R^{i+1}f_{i+1} + {}^{i}F_{i} \qquad (17)$$

$$^{i}n_{i} = {}_{i+1}^{i}R^{i+1}n_{i+1} + {}^{i}P_{C_{i}} \times {}^{i}F_{i} + {}^{i}P_{i+1} \times {}_{i+1}^{i}R^{i+1}f_{i+1} \qquad (18)$$

$$\tau_{gi} = {}^{i}n_{i}^{T}\,{}^{i}\hat{Z}_{i}, \qquad (19)$$

where $^{i}P_{C_{i}}$ is vector locating the COM for the i-th link, $^{i}P_{i+1}$ is vector locating the origin of the coordinate system $i+1$ in the coordinate system i.

The application of the algorithm for robot arm iSoRA results in the equation of gravitational torque vector:

$$G(\theta) = \begin{bmatrix} \tau_{g1} \\ \tau_{g2} \\ \tau_{g3} \\ \tau_{g4} \end{bmatrix} = \begin{bmatrix} L_{M2}m_{2}\left(s_{1}c_{2}c_{4} + c_{1}c_{3}s_{4} + s_{1}s_{2}s_{3}s_{4}\right) + \left(L_{M1}m_{1} + L_{1}m_{2}\right)s_{1}c_{2} \\ L_{M2}m_{2}\left(c_{1}s_{2}c_{4} - c_{1}c_{2}s_{3}s_{4}\right) + \left(L_{M1}m_{1} + L_{1}m_{2}\right)c_{1}s_{2} \\ L_{M2}m_{2}\left(-c_{1}s_{2}c_{3}s_{4} - s_{1}s_{3}s_{4}\right) \\ L_{M2}m_{2}\left(-c_{1}s_{2}s_{3}c_{4} + s_{1}c_{3}c_{4} + c_{1}c_{2}s_{4}\right) \end{bmatrix}\begin{bmatrix} g \\ g \\ g \\ g \end{bmatrix}, \qquad (20)$$

where τ_{gi} is the gravitational torque in i-th joint; m_{1} and m_{2} are the point masses of the first and second link, respectively; L_{M1} and L_{M2} are the distances from the first and second link origins to the centers of mass, respectively; L_{1} is the upper arm length; c_{1}, c_{2}, c_{3}, c_{4}, s_{1}, s_{2}, s_{3}, and s_{4} are abbreviations for $\cos(\theta_{1})$, $\cos(\theta_{2})$, $\cos(\theta_{3})$, $\cos(\theta_{4})$, $\sin(\theta_{1})$, $\sin(\theta_{2})$, $\sin(\theta_{3})$, and $\sin(\theta_{4})$, respectively.

The experiment with the fourth joint of the robot arm was conducted in order to measure the gravity torque (Fig. 18a) and to estimate the error by comparison with reference model (Fig. 18b).

As can be seen from Fig. 18, the pick values of the gravity torque estimation error arise at the start and stop stages of the joint rotation. The reason of this is high inertial loading that provokes the vibrations during acceleration and deceleration transients. This disturbance can be evaluated by using accelerometers and excluded from further consideration. The applied torque while physical contacting with environment is derived by subtraction of gravity term $G(\theta)$ from the sensed signal value. Observing the measurement error plot (Fig. 18b), we can assign the relevant threshold of 0.02 Nm that triggers control of constraint motion.
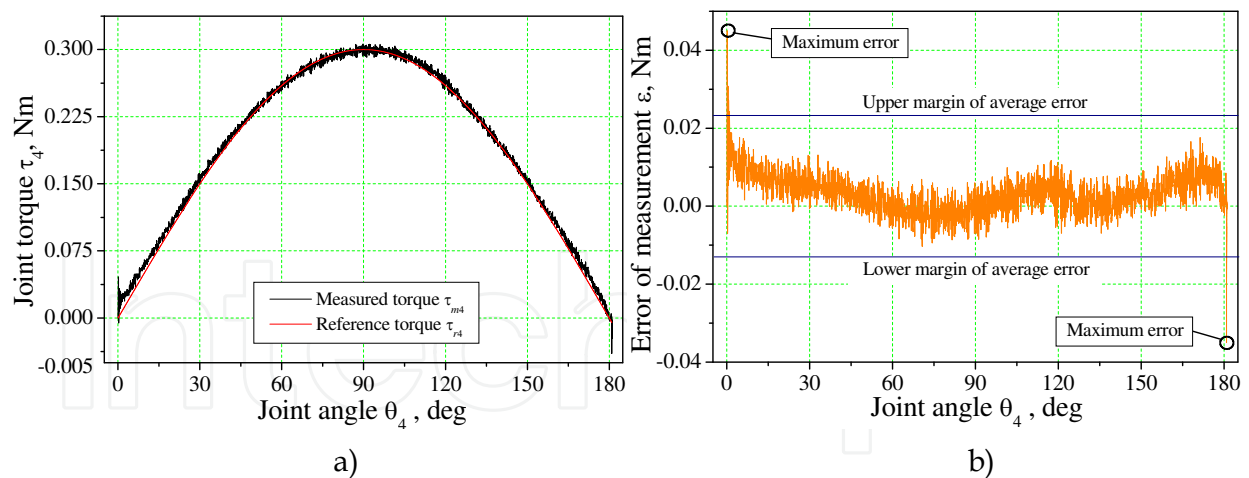
Fig. 18. Experimental results of gravity torque measurement

4.3 Experimental results of joint admittance control

To improve the service task effectiveness, we decided to implement admittance control (Fig. 19). In this case, compliant trajectory generated by the impedance controller is traced by the PD control loop. Thus, inherent dynamics of the robot does not affect the performance of the target impedance model. We adopted K_d = 29 (Nm/rad), D_d = 6.9 (Nm·s/rad), J_d = 0.4 (kg·m²), to achieve closed to critical damped response and sufficient for safe interaction compliance.
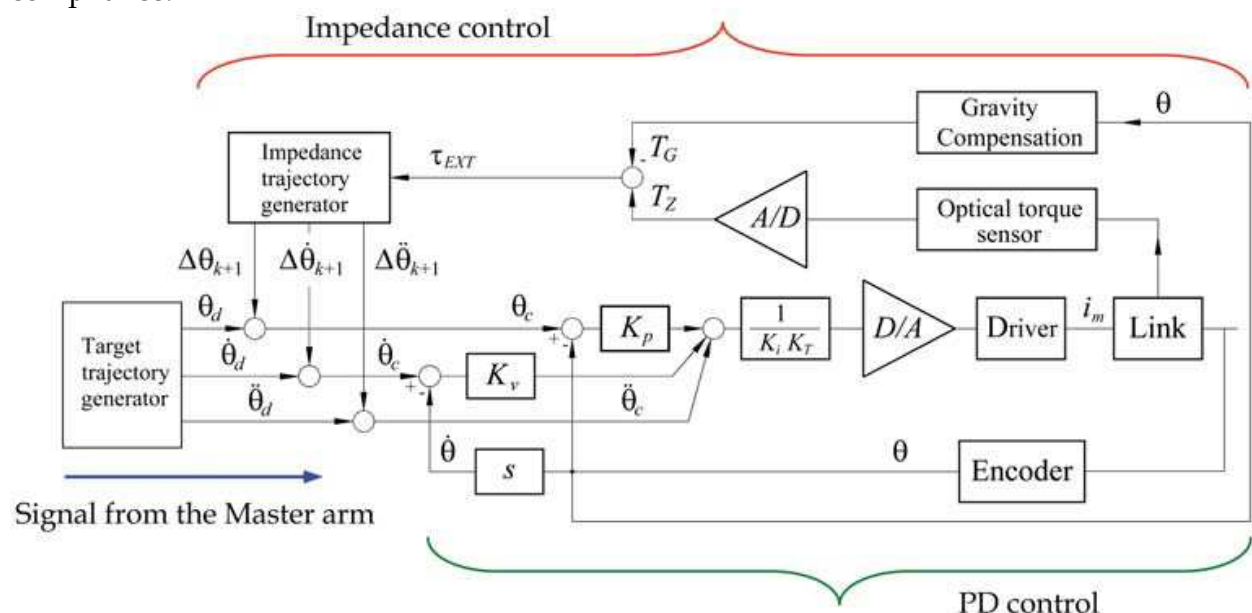
Fig. 19. Block diagram of joint admittance control

To verify the theory and to evaluate the feasibility and performance of the proposed controller, the experiments were conducted with developed robot arm. During the experiment, robot forearm was pushed several times by human in different directions with forces having different magnitude. The experimental results for the elbow joint – applied torque, angle generated by impedance controller, measured joint angle, and error of joint angle in the function of time – are presented in Fig. 20, Fig. 21, Fig. 22 and Fig. 23, respectively.
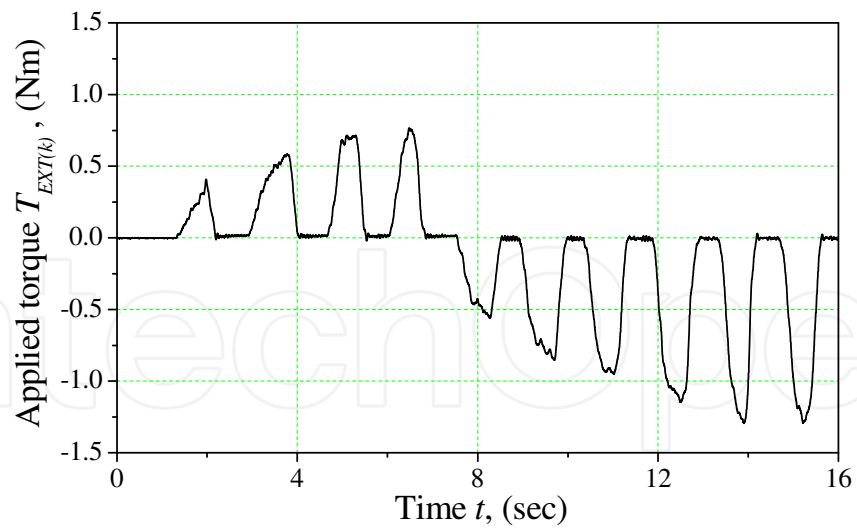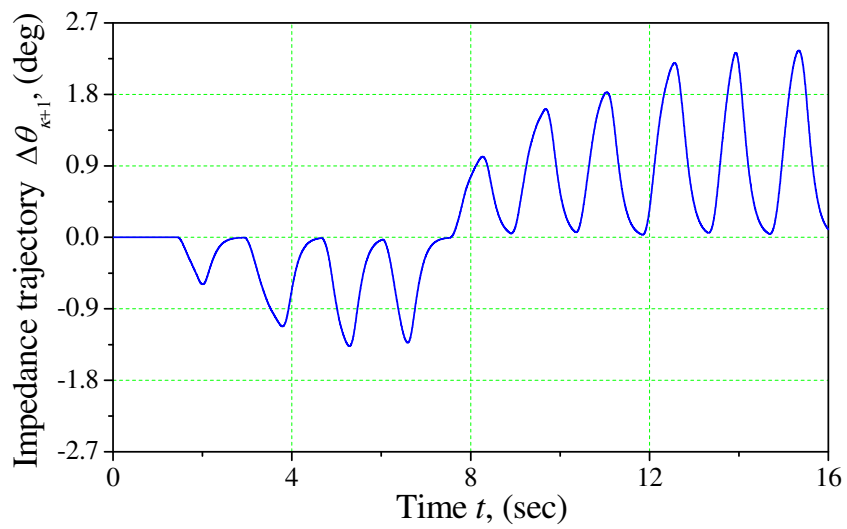
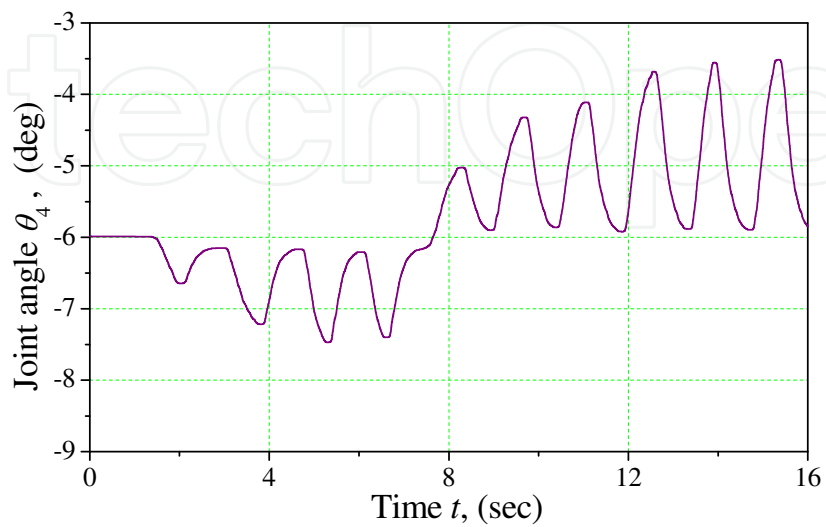Fig. 20. External torque

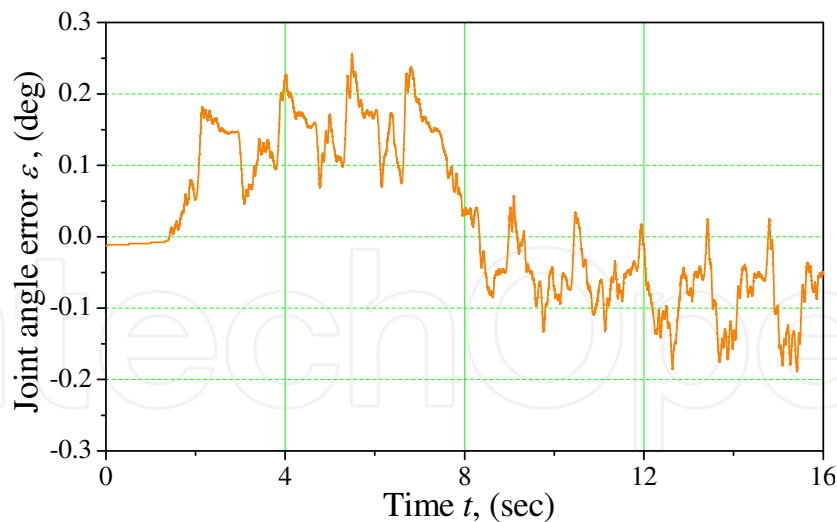Fig. 21. Impedance trajectory

Fig. 22. Measured joint angle

Fig. 23. Joint angle trace error

The experimental results show the successful realization of the joint admittance control. While contacting with human, the robot arm generates compliant soft motion (Fig. 21) according to the sensed torque (Fig. 20). The larger force applied to the robot arm (Fig. 20), the more compliant trajectory is generated by impedance control (Fig. 21).. As we assigned closed to critically damped response of impedance model to disturbance force, output angle ($\Delta\theta_{k+1}$) has ascending-descending exponential trajectory. Admittance control provides small joint angle trace error in borders of -0.2°–0.25° (Fig. 23). The conventionally impedance-controlled robot can realize contacting task only at the tip of the end-effector. By contrast, our approach provides delicate continuous safe interaction of all surface of the robot arm with environment.

5. Conclusion and future work

In Chapter, the stages of the joint torque sensor design are presented. New torque sensors for implementation of virtual backdrivability of robot joint transmissions have been developed. Torque measurement techniques, namely, electrical, electromagnetic, and optical, are discussed in detail. Technical requirements aimed at designing the high-performance torque sensor for humanoid robot arm were formulated. The substantial advantages of the optical technique motivated our choice in its favor. The main novelty of our method is application of the ultra-small size PI as sensitive element to measure relative motion of sensor components. The hub-spoke, ring-shaped, and semi-ring-shaped topologies of the sensor spring member were designed and investigated in order to optimize the mechanical structure of the detector. Hub-spoke structure was proven to be the most suitable solution allowing realization of compact sensor with high resolution. The designed optical torque sensors are characterized by good accuracy, high signal-to-noise ratio, compact sizes, light in weight, easy manufacturing, high signal bandwidth, robustness, low cost, and simple calibration procedure.

In addition to contact force, torque sensor continuously measures the gravity and dynamic load. To extract the value of the contact force from sensor signal, we elaborated algorithm of calculation of torque caused by contact with object.

New whole-sensitive robot arm iSoRA was developed to provide human-like capabilities of contact task performing in a wide variety of environments. Each joint is equipped with optical torque sensor directly connected to the output shaft of harmonic drive. The sizes and appearance of the robot arm were chosen so that the sense of incongruity during interaction with human is avoided. We kept the arm proportions the same as in average height human. The effectiveness of the proposed joint admittance controller ensuring the safety in human-robot interaction was experimentally justified during physical contacting with the entire surface of robot arm body.

Our future research will be focused on elaboration of an approach to estimation of the contact point location, environment stiffness evaluation, and contacting object shape recognition on the basis of knowledge of the applied torques and manipulator geometry.

6. Acknowledgments

7. References

ATI, Multi-Axis Force/Torque Sensor, ATI Industrial Automation, [Online], Available: http://www.ati-ia.com.

Bicchi, A. & Tonietti, G. (2004). Fast and soft arm tactics: dealing with the safety-performance trade-off in robot arms design and control. *IEEE Robotics and Automation Magazine*, Vol. 11, No. 2, (June 2004) 22-33, ISSN 1070-9932

BL AUTOTEC, BL Sensor, BL AUTOTEC, LTD., [Online], Available: http://www.bl-autotec.co.jp.

Fulmek, P. L.; Wandling, F.; Zdiarsky, W.; Brasseur, G. & Cermak, S. P. (2002). Capacitive sensor for relative angle measurement. *IEEE Transactions on Instrumentation and Measurement*, Vol. 51, No. 6, (December 2002) 1145-1149, ISSN 0018-9456

Golder, I.; Hashimoto, M.; Horiuchi, M. & Ninomiya, T. (2001). Performance of gain-turned harmonic drive torque sensor under load and speed conditions. *IEEE/ASME Transaction on Mechatronics*, Vol. 6, No. 2, (June 2001) 155-160, ISSN 1083-4435

Hashimoto, M.; Kiyosawa, Y. & Paul, R. P. (1993). A torque sensing technique for robots with harmonic drives. *IEEE Transaction on Robotics and Automation*, Vol. 9, No. 1, (February 1993) 108-116, ISSN 1042-296X

Hilton, J. A. (1989). Force and torque converter. U. S. Patent 4 811 608, March 1989.

Hirose S. & Yoneda, K. (1990). Development of optical 6-axial force sensor and its signal calibration considering non-linear interference. *Proceedings of IEEE Int. Conf. Robotics and Automation (ICRA)*, pp. 46-53, ISBN 0-8186-9061-5, Cincinnati, May 1990, IEEE Press.

Hirzinger, G.; Albu-Schaffer, A.; Hahnle, M.; Schaefer, I. & Sporer, N. (2001). On a new generation of torque controlled light-weight robots. *Proceedings of IEEE Int. Conf. Robotics and Automation (ICRA)*, pp. 3356-3363, ISBN 0-7803-6576-3, Seoul, May 2001, IEEE Press.

Hogan, N. (1985). Impedance control: an approach to manipulation, Part I-III. *ASME Journal of Dynamic Systems, Measurement and Control,* Vol. 107, (March 1985) 1-23, ISSN 022-0434

Horton, S. J. (2004). Displacement and torque sensor. U.S. Patent 6 800 843, October 2004.

Ishino, R.; Saito, T. & Sunahata. M. (1996). Magnetostrictive torque sensor shaft. U.S. Patent 5 491 369, February 1996.

Kaneko, K.; Kanehiro, F.; Kajita, S.; Hirukawa, H.; Kawasaki, T.; Hirata, M.; Akachi, K. & Isozumu, T. (2004). Humanoid robot HRP 2, *Proceedings of IEEE Int. Conf. Robotics and Automation (ICRA),* pp. 1083-1090, ISBN 0-7803-8233-1, New Orleans, 2004, IEEE Press.

Kovacich, J. A.; Kaboord, W.S.; Begale, F.J.; Brzycki, R.R.; Pahl, B. & Hansen, J.E. (2002). Method of manufacturing a piezoelectric torque sensor. U.S. Patent 6 442 812, September 2002.

Lumelsky, V. J. & Cheung, E. (2001). Sensitive skin. *IEEE Sensors Journal,* Vol. 1, No. 1, (June 2001) 41-51, ISSN 1530-437X

Madni, A. M.; Hansen, R. K. & Vuong, J. B. (2004). Differential capacitive torque sensor. U.S. Patent 6 772 646, August 2004.

Minebea, 6-Axial Force Sensor. Minebea Co., Ltd., [Online], Available: http://www.minebea-mcd.com.

Mitsunaga, N.; Miyashita, T.; Ishiguro, H.; Kogure, K. & Hagita, N. (2006). Robovie IV: A communication robot interacting with people daily in an office, *Proceedings of IEEE/RSJ Int. Conf. Intelligent Robots and Systems (IROS)* pp. 5066-5072, ISBN 1-4244-0259-X, Beijing, October 2006, IEEE Press.

Morikawa, S.; Senoo, T.; Namiki, A. & Ishikawa, M. (2007). Real-time collision avoidance using a robot manipulator with light-weight small high-speed vision system. *Proceedings of IEEE Int. Conf. Robotics and Automation (ICRA),* pp. 794-799, ISBN 1-4244-0602-1, Roma, April 2007, IEEE Press.

Nicot, C. (2004). Torque sensor for a turning shaft. U. S. Patent 6 694 828, February 2004.

Okutani, N. & Nakazawa, K. (1993). Torsion angle detection apparatus and torque sensor. U.S. Patent 5 247 839, September 1993.

ROHM, Photointerrupter design guide. *Product catalog of ROHM,* pp. 6-7, 2005.

Sakagami, Y.; Watanabe, R.; Aoyama, C.; Matsunaga, S.; Higaki, N. & Fujimura, K. (2002). The intelligent ASIMO: System overview and integration, *Proceedings of IEEE/RSJ Int. Conf. on Intelligent Robots and Systems (IROS),* pp. 2478-2483, ISBN 0-7803-7399-5, Lausanne, September 2002, IEEE Press.

Sakaki, T. & Iwakane, T. (1992). Impedance control of a manipulator using torque-controlled lightweight actuators. *IEEE Transaction on Industry Applications,* Vol. 28, No. 6, (November 1992) 1399-1405, ISSN 0093-9994

Shinoura, O. (2003). Torque sensor and manufacturing method of the same. U.S. Patent 6 574 853, June 2003.

Takahashi, N.; Tada, M.; Ueda, J.; Matsumoto, Y. & Ogasawara, T. (2003). An optical 6-axis force sensor for brain function analysis using fMRI, *Proceedings of 2nd IEEE Int. Conf. on Sensors,* Vol. 1, pp. 253-258, ISBN 0-7803-8133-5, Toronto, October 2003, IEEE Press.

Tsetserukou, D.; Tadakuma, R.; Kajimoto, H.; Kawakami, N. & Tachi. S. (2007). Towards safe human-robot interaction: joint impedance control of a new teleoperated robot

arm. *Proceedings of IEEE Int. Symposium on Robot and Human Interactive Communication (RO-MAN)*, pp. 860-865, ISBN 1-4244-1635-6, Jeju island, August 2007, IEEE Press.

Vischer, D. & Khatib, O. (1995). Design and development of high-performance torque controlled joints. *IEEE Transactions on Robotic and Automation*, Vol. 11, No. 4, (August 1995) 537-544, ISSN 1042-296X

Westbrook, M. H. & Turner, J. D. (1994). *Automotive Sensors.* IOF Publishing, ISBN 0750302933, Philadelphia.

Wu, C. H. & Paul, R. P. (1980). Manipulator compliance based on joint torque control, *Proceedings of IEEE Conf. Decision and Control*, pp. 88-94, ISSN 0191-2216, Albuquerque, December 1980, IEEE Press.

Sensors: Focus on Tactile Force and Stress Sensors

Edited by Jose Gerardo Rocha and Senentxu Lanceros-Mendez

This book describes some devices that are commonly identified as tactile or force sensors. This is achieved with different degrees of detail, in a unique and actual resource, through the description of different approaches to this type of sensors. Understanding the design and the working principles of the sensors described here requires a multidisciplinary background of electrical engineering, mechanical engineering, physics, biology, etc. An attempt has been made to place side by side the most pertinent information in order to reach a more productive reading not only for professionals dedicated to the design of tactile sensors, but also for all other sensor users, as for example, in the field of robotics. The latest technologies presented in this book are more focused on information readout and processing: as new materials, micro and sub-micro sensors are available, wireless transmission and processing of the sensorial information, as well as some innovative methodologies for obtaining and interpreting tactile information are also strongly evolving.

How to reference

In order to correctly reference this scholarly work, feel free to copy and paste the following:

Dzmitry Tsetserukou and Susumu Tachi (2008). Torque Sensors for Robot Joint Control, Sensors: Focus on Tactile Force and Stress Sensors, Jose Gerardo Rocha and Senentxu Lanceros-Mendez (Ed.), ISBN: 978-953-7619-31-2, InTech, Available from: http://www.intechopen.com/books/sensors-focus-on-tactile-force-and-stress-sensors/torque_sensors_for_robot_joint_control

INTECH
open science | open minds